Supporting Information

For

High-Throughput Counting and Superresolution Mapping of Tetraspanins on Exosomes using a Single-Molecule Sensitive Flow Technique and Transistor-like Semiconducting Polymer Dots

Yifei Jiang[†], Luca A. Andronico[†], Seung-Ryoung Jung[†], Haobin Chen[†], Bryant Fujimoto[†], Lucia Vojtech[‡], and Daniel T. Chiu[†]*

[†]Department of Chemistry, University of Washington, Seattle, Washington 98195, United States
[‡]Department of Obstetrics and Gynecology, University of Washington, Seattle, Washington 98195, United States

TABLE OF CONTENTS

EXPERIMENTAL SECTION

Line confocal microscope setup

We developed a microfluidics setup based on a line confocal microscope described previously.[1] The system was built on a Nikon TE2000 inverted microscope. Four lasers—405, 488, 561, and 640 nm; 100 mW (Coherent Obis)—were used as excitation sources. Each laser beam was shaped by cylindrical optics to form an elliptical beam. The laser beams were reflected by a multi-band dichroic filter (Chroma, ZT405/488/561/640rpcv2), then were focused onto a microfluidic chip using a 60×, 1.3 NA oil objective. The laser beams typically exhibited 0.5-1.5 μm full-width half-maximum (FWHM) along the microfluidic channel depending on the specific wavelength, and about 20 μm FWHM across the channel. The laser lines were separated evenly by 10 μm. At maximal laser output, the power density inside the channel was ~20 kW/cm^2. A piezo stage (NF15AP25; Thorlabs, Inc.) was used to focus the sample. The fluorescence signal collected by the objective was filtered through an array of rectangular pinholes (National Aperture, Inc.) in the image plane. D-shaped mirrors were placed after the pinholes to split fluorescence detected at different laser lines. For the 640-nm laser line, a dichroic filter was used to separate fluorescence from backscattering signal. Fluorescence and backscattering signals were filtered by bandpass filters before being focused onto avalanche photodiodes (APDs) (SPCM-AQR-14, PerkinElmer, Fremont, CA). The fluorescence filters for Di-8-ANEPPS, Brilliant Violet 510 (BV510), phycoerythrin (PE), and Alexa Fluor 647 were 600/50 nm, 505/20 nm, 609/34 nm, and 690/50 nm, respectively. The autofocusing mechanism was as follows: in each experiment, the objective was first manually focused on the bottom of the channel. Then, based on the channel dimensions, the piezo stage was used to raise the focal plane to the center of the channel. The 640-nm scattering intensity recorded at the channel center by the APD was used as a reference. During the experiment, the piezo stage was driven by the real-time scattering signal to maintain the intensity close to the reference value (<3% difference).

Microfluidic channel fabrication

Details of the microfabrication have been described previously.[1a, 2] Microfluidic channels were designed in AutoCAD (Autodesk) then written onto a chrome photomask (HTA Photomask). Using photolithography, the pattern on the photomask was transferred onto a silicon wafer. The wafer was silanized in a desiccator containing tridecafluoro-1,1,2,2-tetrahydrooctyl-1-trichlorosilane (Sigma-Aldrich) before use as a master to replicate features to polydimethylsiloxane (PDMS). Holes were punched in PDMS at the two ends of the channels to create reservoirs. The PDMS was bonded to a clean cover glass after both were treated with oxygen plasma.

Isolation of seminal exosomes

Semen samples were obtained from the HIV Vaccine Trials Clinic in Seattle. Exosome isolation was performed according to a published protocol[3] approved by the Institutional Review Boards of the University of Washington and the Fred Hutchinson Cancer Research Center. Briefly, a series of centrifugation steps were employed to isolate seminal plasma from semen samples, and the plasma was then filtered through a 0.22-μm syringe filter. After ultracentrifugation over a sucrose gradient, the 30% and 25% sucrose cushions containing seminal exosomes were pooled and washed by centrifugation through an Amicon Ultracel 100-kDa cellulose centrifugal filter. Seminal exosomes were then filtered by a size exclusion chromatography column to remove proteins in solution. The final exosome concentration was ~10^{13}/mL based on nanoparticle tracking analysis.

Flow analysis of seminal exosomes

Prior to labeling, the seminal exosome suspension was diluted to 10^{10}/mL in HEPES buffer (20 mM, pH 7.4). To label tetraspanins, 100 μL of diluted exosome suspension was incubated with 10 μL of diluted antibody solution. For each antibody, we tested multiple concentrations ranging from 10^{-6} to 10^{-1} μg/mL to generate a titration curve. After incubation with antibodies for 1 h, 1 μL of 20 μM Di-8-ANEPPS in dimethyl sulfoxide was added to the solution to label the lipid membrane. After 10 min of incubation with Di-8-ANEPPS, the solution was centrifuged and re-diluted three times in HEPES buffer containing 0.1% bovine serum albumin (BSA) using a spin-column (Sartorius Vivaspin 500, 300-kDA) to remove excess antibodies.

For flow measurements, 5 μL of sample was injected into the inlet reservoir of the microfluidic chip. Due to the height difference of fluid levels in the reservoirs, flow is initiated without an external pump. The typical volumetric flowrate was ~15 pL/s. Fluorescence signals were collected by APDs at 10 kHz. The autofocusing system was engaged to minimize focus drift during the experiment. To differentiate signal from noise, a threshold was set as the average background plus five times the medium absolute deviation of the background. The intensity of each event was calculated by integration within a fixed time window after background subtraction. We collected flow trajectories of diluted free antibodies and Di-8-ANEPPS-labeled exosomes at different excitation powers to determine the optimal signal-to-noise ratio in each channel. For high-throughput tetraspanin profiling, we labeled seminal exosomes with Di-8-ANEPPS and with BV510-anti-CD9 (BD Bioscience, M-L13), PE-anti-CD63 (Thermo Fisher, H5C6), and Alexa Fluor 647-anti-CD81 (Novus, M38) antibodies. Multi-color flow experiments were performed using the optimal excitation setting. The transit time between two laser lines was determined by cross-correlation analysis between the trajectories collected in the corresponding detection channels. The transit time was used to perform colocalization between different channels. Only when an antibody peak occurred within the expected time-window near a membrane dye peak was the signal attributed to an exosome. Non-colocalized antibody peaks were used to generate free antibody distributions. Tetraspanin copy number distributions were obtained by deconvolving the intensity distributions of antibody-labeled exosomes using single antibody intensity distributions.[4]

Pdot preparation and bioconjugation

Poly[(9,9-dihexyl-2,7-(2-cyanodivinylene)-fluorenylenyl-2,7-diyl)] (CN-PDHFV; MW 25,000) and poly[2-methoxy-5-(2-ethylhexyloxy)-1,4-(1-cyanovinylene-1,4-phenylene)] (CN-PPV; MW 13,000) were purchased from ADS Dyes, Inc. Meso-tetraphenyl-tetrabenzoporphine palladium complex (Pd-TPBP) was purchased from AdipoGen, Inc. [6,6]-phenyl C61 butyric acid methyl ester (PCBM), 5,10,15,20-tetraphenyl-21H,23H-porphine zinc (Zn-TPP), poly(styrene-co-maleic anhydride) (PSMA, MW 1,900), tetrahydrofuran (THF, HPLC grade, 99.9%), 1-ethyl-3-(3-dimethylaminopropyl)carbodiimide (EDC), poly(ethylene glycol) (PEG, MW 3,350), bovine serum albumin (BSA), and (3-aminopropyl) trimethoxysilane (APTMS) were purchased from Sigma-Aldrich. All chemicals were used as received without further purification. Pdots were prepared using a nanoprecipitation method described previously.[5] CN-PDHFV, CN-PPV, PCBM, Zn-TPP, Pd-TPBP, and PSMA were dissolved in THF and diluted to 20 ppm. The semiconducting polymers, PCBM, and metalloporphyrins were mixed at various ratios to create precursor solutions of varying dopant percentages (w/w). After thorough mixing, PSMA solution was added to the mixture to make the final precursor containing 10% PSMA (w/w). 2 mL of the precursor solution was rapidly mixed with 8 mL of water under sonication. The mixture was then heated under nitrogen atmosphere to remove THF solvent. After removing THF, the sample was filtered through a 100-nm polyvinylidene fluoride membrane (Millipore) to remove aggregates. The nanoparticle size distribution was determined by dynamic light scattering (DLS). DLS measurements were conducted using a Zetasizer (Malvern Panalytical, UK) at 25 °C with a scattering angle of 173° and an acquisition time of 180 s. UV-vis absorbance and fluorescence spectra were collected using a Beckman Coulter DU720 spectrophotometer and a Perkin Elmer LS55 fluorometer, respectively.

Freshly prepared Pdots were conjugated to antibodies via an EDC-catalyzed reaction.[5c, 6] Anti-CD63 (H5C6) and anti-CD81 (M38) antibodies were purchased from Novus and Thermofisher, respectively. 1 mL of Pdot suspension (~50 μg/mL) was mixed with 20 μL of PEG (5% wt), 20 μL 1 M HEPES buffer, and 20 μL of EDC (5 mg/mL). To produce various Pdot/antibody conjugation ratios, 20, 40, 80, and 120 μL of antibodies (0.5 mg/mL) were added to the mixture. After 4 h of reaction, the solution was centrifuged (Sartorius Vivaspin 500, 300-kDA) and re-diluted three times in HEPES buffer containing 0.2% BSA (w/v). The final solution was concentrated to 0.5 mL and loaded into a size-exclusion column packed with Sephacryl S-400 HR resin; 20 mM HEPES with 0.1% PEG was used as buffer. Purified Pdots were collected from the colored band eluate from the column. To verify the Pdot/antibody conjugation ratio, we used Alexa Fluor 647-conjugated secondary antibodies to label the Pdots and performed multi-color imaging with a microscope. We found that 1 mL of Pdot and 20 μL of antibody yielded mostly non-labeled and ~20% single antibody-conjugated Pdots.

Single-particle and superresolution imaging

Single-particle and superresolution imaging was performed using a custom wide-field microscope (Nikon, TE2000-U) described previously.[7] The excitation sources were a 405-nm laser (Coherent,

Obis, 50 mW), a 488-nm laser (Coherent, Sapphire, 100 mW), a 532-nm laser (Roithner, 50 mW), and a 640-nm laser (Coherent, Obis, 100 mW). A multi-band dichroic filter (Chroma, ZT405/488/532/640rpc-XT) was used to reflect excitation light to the objective (Nikon, Plan Apo TIRF, 100×, 1.45 NA, oil). The full-width half-maxima of the laser profiles were ~30–40 μm at the sample plane. The emission filters used for CN-PDHFV/10% Pd-TPBP/20% PCBM and CN-PPV/10% Zn-TPP/20% PCBM Pdots were 525/50 nm and 660/80 nm, respectively. The filtered emission light passed through a cylindrical lens before focusing onto a sCMOS camera (Hamamatsu, Orca flash 4.0). The detector settings were 16 bits per pixel, 0.5 gain, rolling shutter mode. Imaging of a TEM calibration grid yielded a pixel pitch of 110 nm/pixel.

To prepare single-particle imaging samples, diluted Pdot or Alexa Fluor 647-conjugated antibody suspension was drop-cast onto coverslips functionalized with APTMS. Single particle/dye imaging was performed in oxygen-scavenging glucose oxidase (GLOX) buffer contain 0.5% beta-mercaptoethanol (BME) (Sigma-Aldrich) for 600 s using a frame rate of 50 Hz. The typical excitation power density was ~2 kW/cm^2 at the center of the laser spot. The power density of the 405-nm activation laser was adjusted to 30, 60, 120, 240, and 480 W/cm^2 to evaluate the efficiency of photoactivation. Single-particle localization of the Pdots was performed using a custom MATLAB (MathWorks) script. To differentiate Pdots or Alexa Fluor 647 from background noise, the script used 5–10% of the intensity of the brightest pixel of all frames as a threshold. Initial single-particle localization was performed by searching for pixels above the threshold frame by frame and comparing their intensities to the adjacent pixel. The precise position of a Pdot or Alexa Fluor 647 was then determined by nonlinear least-squares fitting of a Gaussian function to the point spread functions (PSFs). Typically 7×7 pixels were used for the fitting (three pixels on each side of the central pixel). The script then checked the FWHM obtained from the fitting to rule out the possibility of multiple adjacent Pdots or large aggregates.

To prepare superresolution imaging samples, seminal exosomes (10^{10}/mL) was incubated with antibody/Pdot cocktail for 1 h, then filtered through a size exclusion column (IZON, 35 nm). 100 μL of the filtered sample was mixed with 1 μL of 50 μM PKH-26 (Sigma-Aldrich) and incubated for 20 min, then washed/concentrated by centrifugation through an Amicon Ultra-4 100-kDa column. The exosomes were immobilized on poly-L-lysine-coated 8-well chambered slides (Ibidi, 80821) and was then washed with 20 mM HEPES three times and submerged under GLOX buffer containing 0.5% BME. Imaging and bleaching of PKH-26 were performed at the beginning of the experiment for exosome density estimation and downstream multi-color colocalization. Multi-color superresolution imaging was performed sequentially. A commercial autofocus system (ASI CRIFF) was used to keep the system in focus during imaging. The experimental framerate was set to 50 Hz. The typical excitation power density was ~2 kW/cm^2 at the center of the laser spot. The activation laser intensity was adjusted according to the copy number to ensure appropriate activation fraction. Typically, to resolve the localization histogram of a single probe, at least ~50 localization points are required. Under our experimental condition, approximately 0.1 localization point was recorded per exosome, per frame. Based on the average tetraspanin copy number determined by flow analysis, in order to resolve the spatial distributions of CD63, CD81, and CD9,

at least 6400, 800, and 8500 frames are required, which correspond to 128, 16, and 170 seconds of imaging time, at 50 Hz framerate, respectively. The images were analyzed using the ThunderSTORM plugin in ImageJ as follows. Similar to the localization method described above, a peak search threshold was set to five times the background noise fluctuation level for the initial localization. The precise lateral position of a Pdot or Alexa Fluor 647 was determined by fitting the PSF to an elliptical Gaussian function. Typically 7×7 pixels were used for the fitting (three pixels on each side of the central pixel). The FWHMs along the two axes were used to determine the axial position. Frame by frame subtraction analysis was performed to reduce clustering artifact. For each type of label, the relationship between the aspect ratio of the PSF and the axial position was determined by imaging the corresponding label immobilized on a cover glass. A PIEZO stage (Thorlabs, APB302) was employed to scan through multiple axial positions and monitored changes in PSFs throughout the process. The PSF width versus axial position data were fit to a polynomial function and imported to ImageJ to be stored as a calibration standard. We employed the cross-correlation drift-correction method provided by ThunderSTORM to correct for lateral drift during the experiment. Briefly, the image stacks were divided into small segments to construct superresolution images. Cross-correlation analysis was performed between the superresolution images of different segments to determine the lateral drift over time. For multi-color imaging, since the interval between the individual measurements was short, the drift-correction functions obtained from the individual runs were combined to determine the lateral drift of the entire experiment, which was used to generate the overlay plot.

SUPPORTING RESULTS AND DISCUSSION

Flow intensity trajectories of Di-8-ANEPPS-labeled exosomes and Di-8-ANEPPS in HEPES buffer

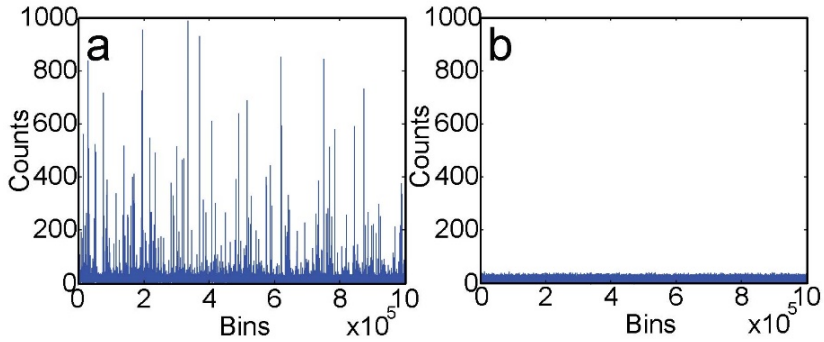

Figure S1. Flow intensity trajectories of a) 200 nM Di-8-ANEPPS-labeled exosomes and b) 200 nM Di-8-ANEPPS in HEPES buffer.

Cross-correlation and colocalization between different channels

To obtain optimal signal-to-noise ratio and minimize crosstalk between the detection channels, the four laser lines were evenly separated by 10 μm. As a result, when a membrane dye and antibody-labeled exosome flowed pass the laser lines, there were time offsets for fluorescence signals detected by different detectors. Typically, the linear velocity is consistent throughout the experiment such that we can use cross-correlation between the fluorescence trajectories collected by the different detectors to determine the transit time. From the correlation peak, we determined that the typical transit time between adjacent laser lines was 2 ± 1.8 ms (Figure S2a). According to the transit time distribution, we performed multi-color colocalization between the different detection channels. Only when an antibody peak occurred within the expected time-window near a membrane dye peak was the signal attributed to an exosome, thus minimizing the influence of free antibodies (Figure S2b). When there was no correlation between events in the different detection channels (for example, in a control containing a multi-color antibody cocktail without exosomes), no peaks were observed in the cross-correlation plot, indicating that peaks in the different detection channels were separated by random time intervals. This served as a convenient and robust way to determine whether the exosomes were successfully labeled by the antibodies.

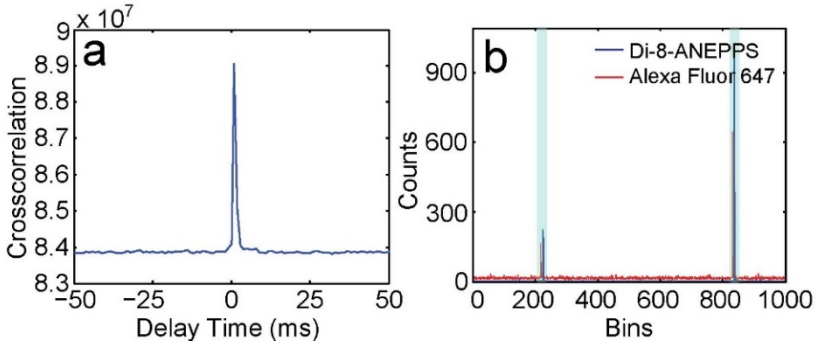

Figure S2. a) Cross-correlation plot between exosome flow trajectories acquired by two detection channels. b) Zoomed-in view of the corresponding flow trajectories with colocalized events highlighted by blue bands.

Deconvolution analysis

Deconvolution analysis was performed as we described previously.[4, 8] Briefly, the free antibody distribution was fitted to a log-normal distribution. By multiplying the fitted distribution by 1, 2, 3,…, n, we generated a set of distributions $I_1, I_2, I_3, \ldots, I_n$ which correspond to the intensities of 1, 2, 3,…, n antibodies. The population of each set was varied to reproduce the intensity distribution of antibody-labeled exosomes and minimize the fitting residue. The average copy number was estimated by dividing the average intensity of the antibody-labeled exosomes by the average single antibody intensity, to provide a starting point for deconvolution. The intensity distribution, deconvolution fit curve, and fitting residues of $CD63^+$, $CD81^+$, and $CD9^+$ exosomes are shown in Figure S3.

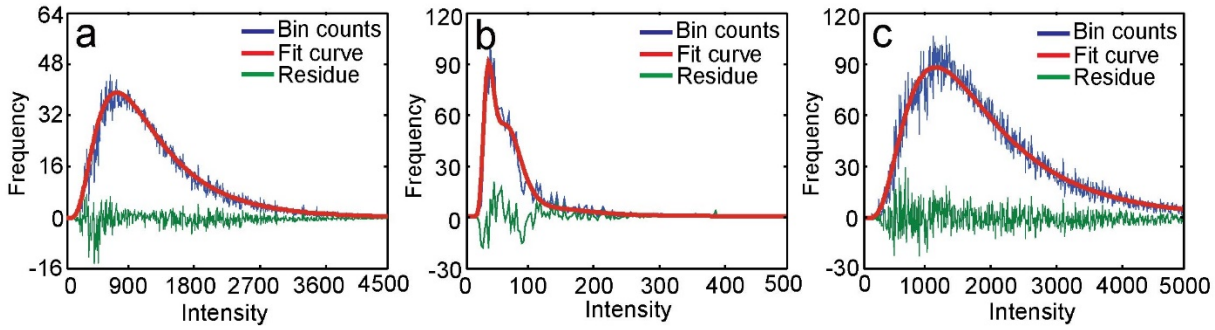

Figure S3. a-c) Intensity distributions, deconvolution fit curves, and fitting residues of a) CD63+, b) CD81+, and c) CD9+ exosomes.

Titration curves

To ensure saturated labeling we used various antibody concentrations to label the exosomes. As antibody concentration increased, the colocalization (labeled) percentage and copy number determined from flow typically increased monotonically before reaching a plateau (Figure S4a-f). The labeled percentage was determined by dividing the number of colocalized events (antibody-labeled exosomes) by the total number of Di-8-ANEPPS-positive events. From the titrations, we determined that under saturated labeling the average copy numbers of CD63, CD81, and CD9 were 12.8, 1.6, and 17.0, respectively. The percentages of $CD63^+$, $CD81^+$, and $CD9^+$ exosomes were 28%, 5%, and 33.5%, respectively.

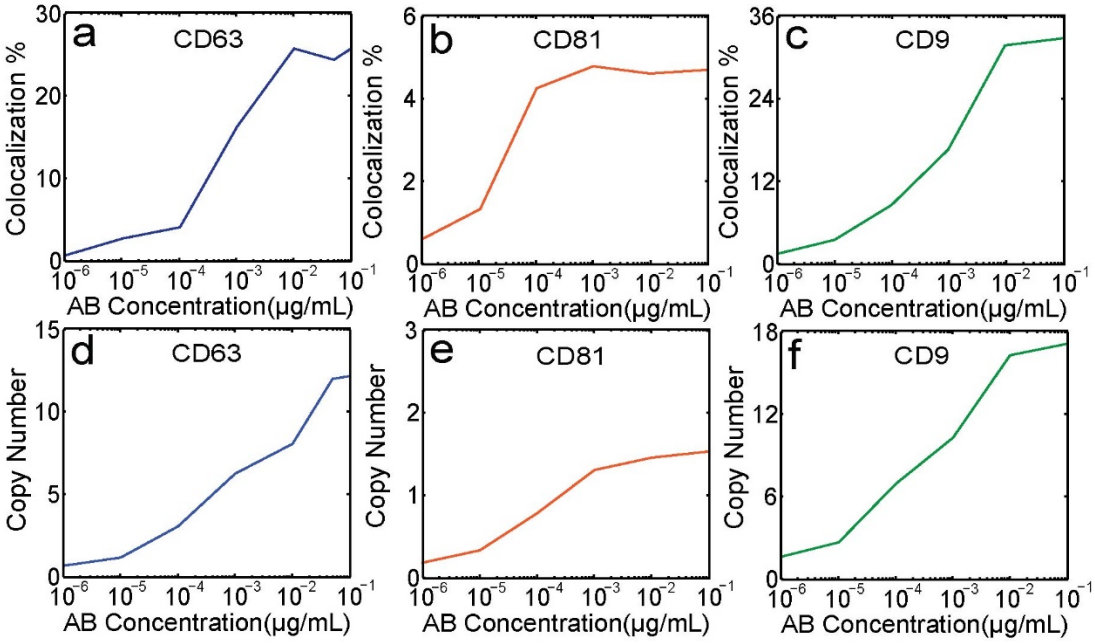

Figure S4. Expression percentage and copy number of a, d) CD63, b, e) CD81, and c, f) CD9 versus antibody concentration, determined from flow analysis.

Fluorescence microscopy images of Pdot photoactivation

The switch-on fraction (duty cycle) of the Pdots under different activation intensities was measured using a method described previously.[7] Briefly, since hole polaron generation is a photo-driven process, all Pdots were switched on when first exposed to 488-nm excitation, which was used to determine the total number of Pdots in the region of interest (ROI). The duty cycle gradually decreased until it reached equilibrium. Depending on the 488-nm excitation power, this process could take up to tens of seconds. At the equilibrium, low-frequency switch on events can be observed due to stochastic fluctuation in the hole population, as reported previously.[7] Exposure to 405-nm excitation significantly increased the duty cycle, i.e., an increased number the Pdots were switched on per frame (Figure S5). The activation effect increased with the 405-nm excitation power. At each activation intensity, the duty cycle was calculated by the averge number of Pdots switched on per frame by the total number of Pdots in the ROI.

To optimize the Pdot composition, for each dopant, we tested 4 doping percentages (5%, 10%, 20%, 40%), which yielded 16 combinations in total. Using the single-particle imaging method described above, we characterized the on-state photon number, photoswitching duty cycle and photoactivation responses of each combination. It was observed that, at low PCBM doping level (<10%), some Pdots do not completely turn off due to insufficient number of photo-generated quenchers. For Pdots doped with 20% PCBM, robust photoswitching can be observed and the duty cycle is suitable for superresolution imaging (~0.002). Upon further increase of the PCBM doping

level (40%), the switch-on frequency of the Pdots became too low for efficient imaging. Among all the 20% PCBM doped Pdots, the one that contained 10% metalloporphyrin exhibited the strongest photoactivation response. Further increase of the metalloporphyrin doping percentage resulted in less efficient photoactivation, likely due to aggregation-induced self-quenching of the dopants inside the Pdots. Based on these results, we chose to use 10% metalloporphyrin and 20% PCBM doped Pdots for superresolution imaging of exosomes.

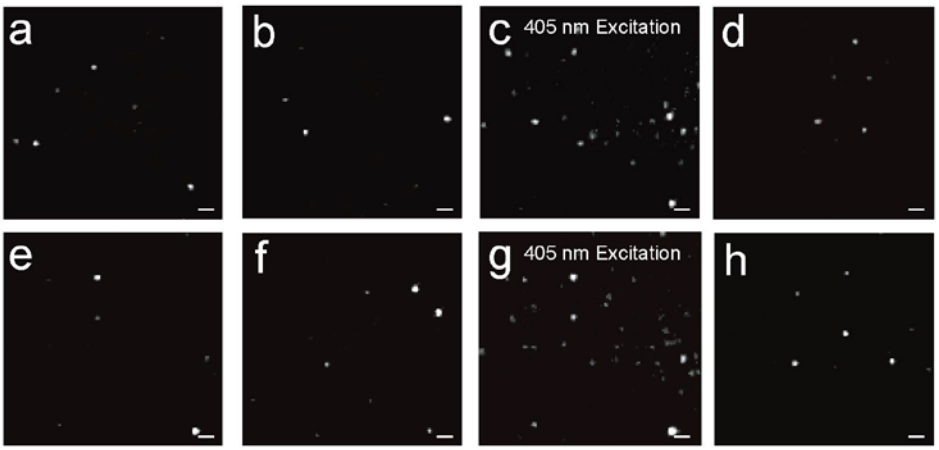

Figure S5. A sequence of fluorescence microscopy images of 10% CN-PPV/10% Zn-TPP/20% PCBM Pdots, showing a, b, d-f, h) stochastic blinking under equilibration, and c, g) activation by 405-nm excitation. Scale bar: 1μm.

Chemical structures and energy levels

The Pdots were designed according to the principles of N-P-N transistors. Semiconducting polymer was used as the host matrix, PCBM as the electron drain, and metalloporphyrins as the electron source. Under 488-nm excitation, electrons are transferred from conjugated polymers to PCBM and metalloporphyrins. While the reaction occurs both ways, electron transfer to PCBM is likely the dominating pathway, considering the lower-lying energy levels of PCBM. The accumulated holes in the semiconducting polymer phase results in almost complete quenching of the Pdot emission. Low-frequency switch-on events can be observed due to stochastic fluctuations in the hole population. When the metalloporphyrin is excited to the higher excited state by a 405-nm laser, due to the favorable energy level alignment, it efficiently transfers electron back to the semiconducting polymer, which temporarily reduces hole population in the polymer phase and activates Pdot emission. In general, if semiconducting polymers and dopant molecules in Pdots form a staggered energy level alignment, photoswitching and photoactivation behavior is expected. For example, we previously designed a class of Pdots with staggered energy levels formed by P- and N-type semiconducting polymers and observed similar photoswitching/photoactivation behavior.[7] Similarly, Pdots can be doped with various other types of molecules that can undergo photo-induced electron transfer reaction with semiconducting polymers. The exact performance

of the Pdots is dictated by the offset between the energy levels as well as the dispersion homogeneity of the dopant molecules, both of which can affect electron-transfer efficiency. In addition, because higher excited-state dynamics is involved, there is a competition between higher excited-state electron transfer and internal conversion. In order to achieve strong photoactivation effect, it is necessary to optimize the alignment of the corresponding energy levels to ensure that there is an efficient higher excited-state electron-transfer pathway. Metalloporphyrins were chosen in this study to enhance the activation effect as they are among a small number of molecules that display an recordable anti-Kasha fluorescence from the higher excited state and have been widely exploited to study higher excite state electron transfer. [9] Indeed, by optimizing the doping percentage, we obtained a class of Pdots that exhibited much stronger activation effect with a broad range of adjustable duty cycles (0.0015–0.1).

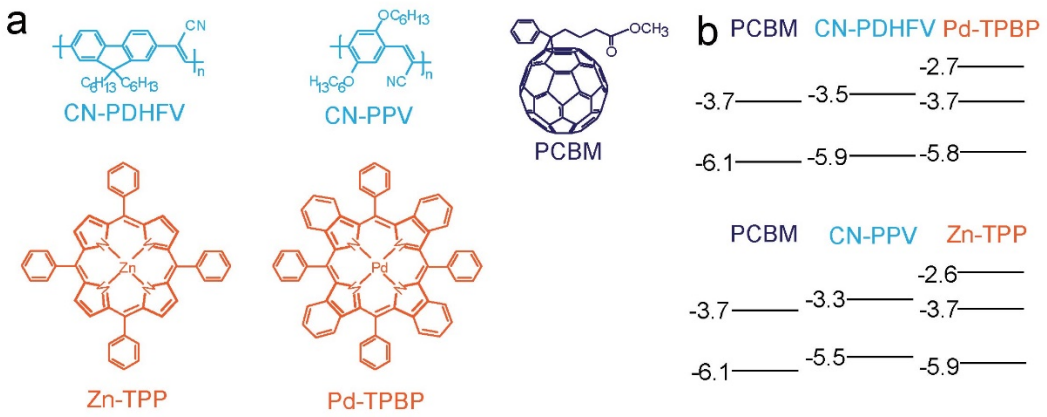

Figure S6. a) Chemical Structures and b) previously reported energy levels of CN-PDHFV,[10] CN-PPV,[11] PCBM,[12] Zn-TPP,[13] and Pd-TPBP.[14]

Photon number histograms and localization precision determination

The lateral localization uncertainty of a single fluorescent probe is related to shot noise and the optical characteristics of the imaging system, which is given by[15]

$$\sigma = \sqrt{\frac{s^2}{N} + \frac{\alpha^2/12}{N} + \frac{8\pi s^4 b^2}{\alpha^2 N^2}}, \quad (1)$$

where s is the standard deviation of the PSF, α is the pixel size, b is the background noise, and N is the detected photon number per switching cycle. The standard deviation of the Pdots or Alexa Fluor 647 PSF is ~130 nm. The pixel size of our setup is 110 nm. The background noise under the typical imaging condition is 5–20, which has contributions from readout noise, background autofluorescence, and scattered light. For the CN-PDHFV/10% Pd-TPBP/20% PCBM Pdots, 10% CN-PPV/10% Zn-TPP/20% PCBM Pdots and Alexa Fluor 647, the average photon numbers per switching cycle were 1.1×10^4, 8.8×10^3, and 5.0×10^3, respectively (Figure S7). Based on these

photon numbers and a background noise of 10, the calculated theoretical localization uncertainties for the three probes were 1.4, 1.6, and 2.5 nm, respectively. The experimental localization uncertainty is typically higher due to additional errors introduced in drift correction as well as small focus drifts during the experiment.

The experimental localization uncertainties were obtained from imaging Pdots and Alexa Fluor 647-conjugated antibodies immobilized on a glass coverslip. The lateral position was determined from the fluorescence centroid, whereas the axial position was determined from the width of the PSF along the two axes. For each Pdot, we obtained a cluster of localized positions (Figure S8a). The localization uncertainties along the X, Y, and Z axes were determined from the standard deviations of the localization histograms obtained from dozens of Pdots (Figure S8b-d). The overall lateral localization precision was given by $(\sigma_x + \sigma_y)/2$. Typically, the axial localization uncertainty was around two times the lateral localization uncertainty, consistent with previously results of the astigmatism method (Table S1).[16] By analyzing localization clusters of Pdots in exosome imaging, we estimated that the localization precision of Pdots on exosome was close to the localization precision obtained on glass, with <10% difference.

Table S1. Experimental localization uncertainties of Pdots

	CN-PDHFV/10% Pd-TPBP/20% PCBM Pdots	10% CN-PPV/10% Zn-TPP/20% PCBM Pdots	Alexa Fluor 647
Experimental lateral uncertainty (nm)	4.4	5.0	10.4
Experimental axial uncertainty (nm)	9.0	10.2	20.9

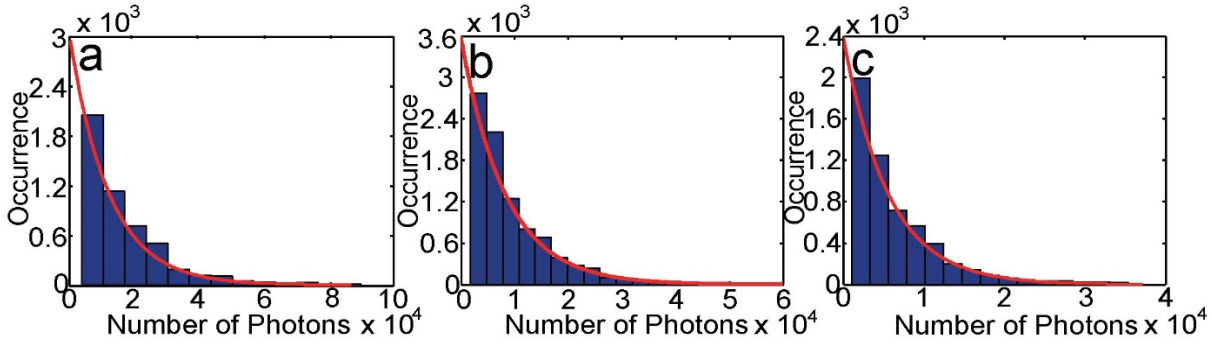

Figure S7. a-c) "On" event photon number histograms of a) CN-PDHFV/10% Pd-TPBP/20% PCBM Pdots, b) 10% CN-PPV/10% Zn-TPP/20% PCBM Pdots, c) Alexa Fluor 647. The red lines represent single exponential fits to the distributions.

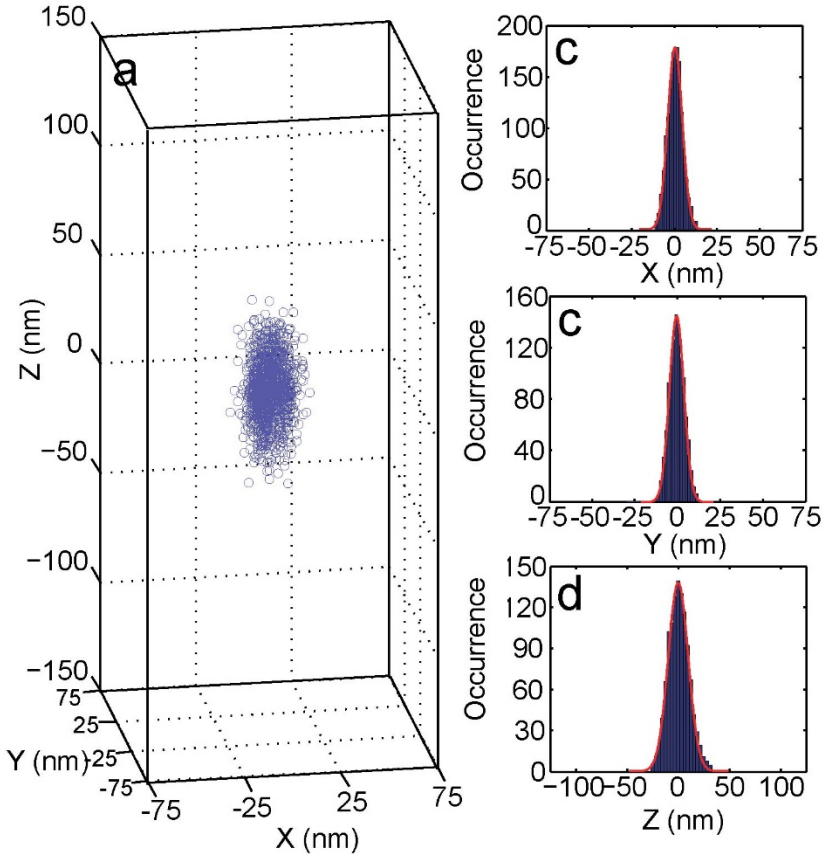

Figure S8. a) 3D scatter plot of localized positions of 10% CN-PPV/10% Zn-TPP/20% PCBM Pdots immobilized on a glass coverslip. b-d) Localization position histogram of CN-PDHFV/10% Pd-TPBP/20% PCBM Pdots along the b) X-, c) Y-, and d) Z-axes, fit to Gaussian distributions with standard deviations of 4.8, 5.2, and 10.2, respectively.

Calibration curve for 3D astigmatism microscopy

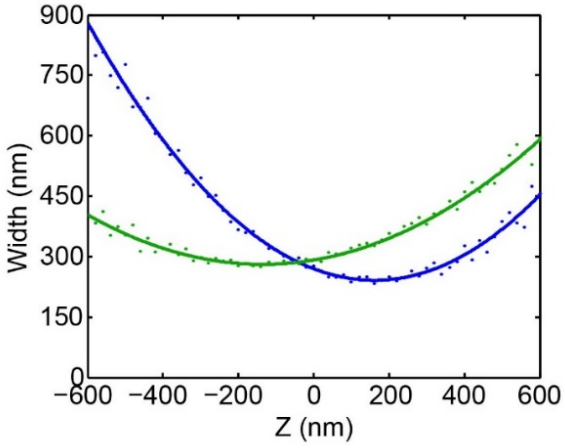

Figure S9. Calibration curve of PSF widths along X- (blue) and Y- (green) axes, at different axial positions, obtained from imaging undoped CN-PDHFV Pdots immobilized on a glass coverslip. Each data point represents the average value of 25 Pdots.

Superresolution image analysis

To determine the percentages of exosome subgroups from imaging, we first counted the total number of exosomes from the membrane dye imaging channel. Then, the number of $CD63^+$, $CD9^+$, and $CD81^+$ exosomes were counted from the corresponding antibody/Pdot imaging channels (Figure S10a-c). Different subgroups of exosomes were identified from the multi-color colocalization analysis. The percentage of each subgroup was given by the number of exosomes in the subgroup divided by the total number of exosomes in the ROI. Non-specific binding of the Pdots and Alexa Fluor 647-conjugated antibodies on the glass surface could result in random colocalization between the membrane dye and Pdots/Alexa Fluor 647 detection channels. The non-specific binding density of each label on the glass surface was calculated from the areas with no membrane dye spots. From the averaged exosome size and the non-specific binding densities, we calculated the expected random colocalization percentages, which were 0.5-1% for the Pdots and 0.05% for the Alexa Fluor 647-conjugated antibodies. The random colocalization effect mostly affect exosomes that express only one of the tetraspanins. To determine the actual expression percentages, the expected random colocalization percentages were subtracted from the raw expression percentages determined from the colocalization analysis (Figure S10d).

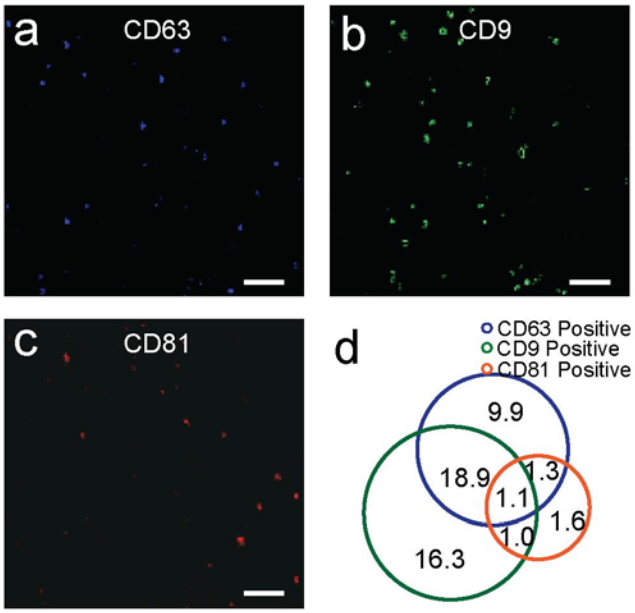

Figure S10. a-c) Superresolution lateral slices of a) $CD63^+$, b) $CD9^+$, and c) $CD81^+$ seminal exosomes. Scale bar: 1μm. d) Percentages of different subpopulations of seminal exosomes, determined from superresolution image analysis.

Size broadening caused by immunoglobulin G (IgGs) antibodies was a commonly observed artifacts in superresolution imaging.[17] In superresolution study of microtubules (MTs), it was observed that dye conjugated antibody labeled MTs yielded a diameter of 34–36 nm, while the MT diameter measured from electron microscopy was ~26 nm, indicating that a single layer of IgGs can increase MT diameter by 8–10 nm. [17b] Similarly, labeling with IgG antibodies and Pdots can increase exosome size measured from superresolution imaging (Figure S11a). For each exosome, we plotted lateral slices at a series of axial positions (20-nm separation) to roughly determine the exosome center along the Z axis. The central slices with ring-shaped structures were fitted to circles to determine the size and the lateral center of the exosome (Figure S11b). To account for the broadening artifacts, the uncorrected exosome sizes measured from Alexa Fluor 647 labeled exosomes were subtracted by 8 nm to yield the actual exosome sizes. Pdots labeled exosome has additional broadening artifacts induced by the size of Pdots. As shown in Figure S11c, for an exosome labeled with both Alexa Fluor 647 and Pdots, the line scans showed that Pdots labeling increase the exosome size by another 13 nm, consistent with the Pdot size measured by DLS. Overall, for Pdots labeled exosomes, the measured size from images were subtracted by 20 nm to account for the sizes of both IgGs and Pdots.

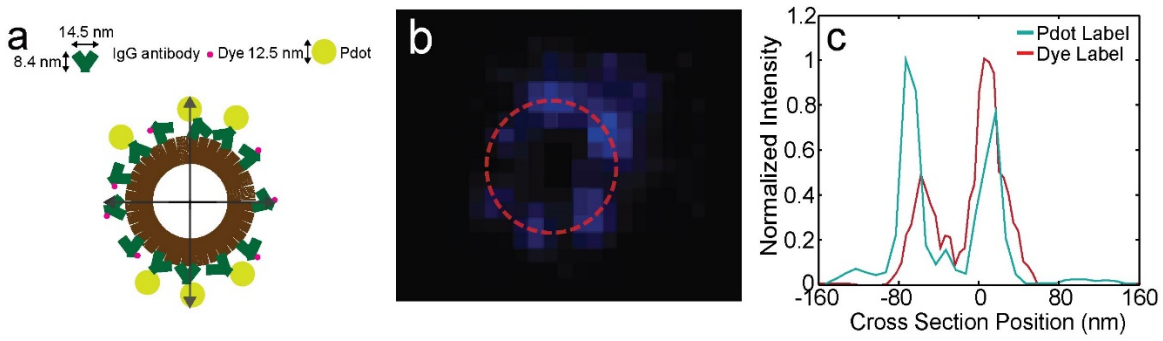

Figure S11 a) Schematic illustration of cross-section of a single exosome labeled with both Pdot and dye-conjugated IgG antibodies. b) A lateral slice of an exsome superresolution image, fitted to a circle.c) Superresolution line scan of a single exosome labeled by both Pdot (cyan) and Alexa-647 (red).

To visualize the 3D spatial distribution of the tetraspanins on an exosome, we grouped the localization points into 4×4×4 nm cells and plotted them using a color-coded 3D scatter plot, in which the color indicates the localization event number of a cell (Figure S12a). The scatter plot was then analyzed using a 3D peak-finding algorithm. The peak search threshold was set to 30% of the expected localization event number within the central cell of a localization cluster. The cells above the threshold were compared with the neighboring cells to locate local maxima and determine the number of clusters in the image. The precise position of a protein was calculated by averaging over all the localization points in the central and the neighboring cells within the cluster. To calculate the surface distance between the proteins, the protein positions were linked with the center of the exosome to calculate the central angles, which were then converted to surface distance by multiplying by the radius of the exosome. As discussed above, for exosomes that express only

one of the tetraspanins, there is minor influence from random colocalization caused by the non-specific binding of the Pdots and Alexa Fluor 647-conjugated antibodies on the glass surface. For CD63 and CD9, such effect is easy to distinguish, as the random colocalization only occurs at the bottom slice of the 3D images and the exosome only has one copy of the protein. For CD81, due to the low expression level, it is difficult to differentiate CD81 positive exosomes from randomly colocalized exosomes. For copy number calculation, we estimated the contribution from random colocalization based on non-specific binding density and subtracted it from the raw copy number histogram of CD81. After the correction, we determined the copy number of CD63, CD81, and CD9 to be 12.6, 1.6, and 16.6, respectively, which is consistent with the copy numbers determined from the flow analysis (Figure S12b, c, d).

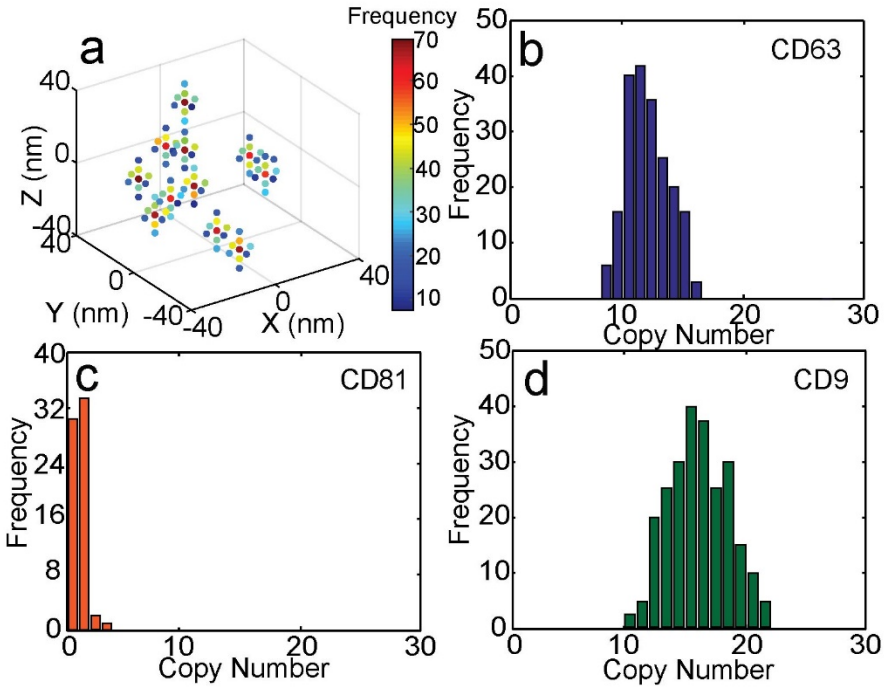

Figure S12.a) The 3D color-coded scatter plot of the CD63 localization clusters on an exosome. b-d) Copy number distribution of b) CD63, c) CD9, and d) CD81, determined from imaging analysis.

REFERENCES

[1] a) P. G. Schiro, C. L. Kuyper, D. T. Chiu, *Electrophoresis* **2007**, *28*, 2430-2438; b) S.-R. Jung, R. Han, W. Sun, Y. Jiang, B. S. Fujimoto, J. Yu, C.-T. Kuo, Y. Rong, X.-H. Zhou, D. T. Chiu, *Anal. Chem.* **2018**, *90*, 6089-6095.

[2] R. M. Lorenz, G. S. Fiorini, G. D. Jeffries, D. S. Lim, M. He, D. T. Chiu, *Anal. Chim. Acta* **2008**, *630*, 124-130.

[3] L. Vojtech, S. Woo, S. Hughes, C. Levy, L. Ballweber, R. P. Sauteraud, J. Strobl, K. Westerberg, R. Gottardo, M. Tewari, *Nucleic Acids Res.* **2014**, *42*, 7290-7304.

[4] S. A. Mutch, J. C. Gadd, B. S. Fujimoto, P. Kensel-Hammes, P. G. Schiro, S. M. Bajjalieh, D. T. Chiu, *Nat. Protoco.* **2011**, *6*, 1953-1968.
[5] a) Y. Jiang, J. McNeill, *Chem. Rev.* **2017**, *117*, 838-859; b) C. Wu, C. Szymanski, J. McNeill, *Langmuir* **2006**, *22*, 2956-2960; c) C. Wu, T. Schneider, M. Zeigler, J. Yu, P. G. Schiro, D. R. Burnham, J. D. McNeill, D. T. Chiu, *J. Am. Chem. Soc.* **2010**, *132*, 15410-15417.
[6] C. Wu, S. J. Hansen, Q. Hou, J. Yu, M. Zeigler, Y. Jin, D. R. Burnham, J. D. McNeill, J. M. Olson, D. T. Chiu, *Angew. Chem. Int. Ed.* **2011**, *50*, 3430-3434.
[7] Y. Jiang, Q. Hu, H. Chen, J. Zhang, D. T. Chiu, J. D. McNeill, *Angew. Chem. Int. Ed.* **2020**, *59*, 16173-16180.
[8] S. A. Mutch, P. Kensel-Hammes, J. C. Gadd, B. S. Fujimoto, R. W. Allen, P. G. Schiro, R. M. Lorenz, C. L. Kuyper, J. S. Kuo, S. M. Bajjalieh, *J. Neurosci.* **2011**, *31*, 1461-1470.
[9] a) M. Andersson, J. Davidsson, L. Hammarström, J. Korppi-Tommola, T. Peltola, *J. Phys. Chem. B* **1999**, *103*, 3258-3262; b) K. Kiyosawa, N. Shiraishi, T. Shimada, D. Masui, H. Tachibana, S. Takagi, O. Ishitani, D. A. Tryk, H. Inoue, *J. Phys. Chem. C* **2009**, *113*, 11667-11673; c) A. P. Demchenko, V. I. Tomin, P.-T. Chou, *Chem. Rev.* **2017**, *117*, 13353-13381.
[10] Y. Aoki, M. Shakutsui, K. Fujita, *Thin Solid Films* **2009**, *518*, 493-496.
[11] Y. Li, Y. Cao, J. Gao, D. Wang, G. Yu, A. J. Heeger, *Synth. Met.* **1999**, *99*, 243-248.
[12] X. He, F. Gao, G. Tu, D. G. Hasko, S. Hüttner, N. C. Greenham, U. Steiner, R. H. Friend, W. T. Huck, *Adv. Funct. Mater.* **2011**, *21*, 139-146.
[13] T. Oku, T. Noma, A. Suzuki, K. Kikuchi, S. Kikuchi, *J. Phys. Chem. Solids* **2010**, *71*, 551-555.
[14] T. Oku, K. Kumada, A. Suzuki, K. Kikuchi, *Open Eng.* **2012**, *2*, 248-252.
[15] R. E. Thompson, D. R. Larson, W. W. Webb, *Biophys. J.* **2002**, *82*, 2775-2783.
[16] B. Huang, W. Wang, M. Bates, X. Zhuang, *Science* **2008**, *319*, 810-813.
[17] a) Y. H. Tan, M. Liu, B. Nolting, J. G. Go, J. Gervay-Hague, G.-y. Liu, *ACS Nano* **2008**, *2*, 2374-2384; b) G. T. Dempsey, J. C. Vaughan, K. H. Chen, M. Bates, X. Zhuang, *Nat. Methods* **2011**, *8*, 1027-1036; c) J.-B. Chang, F. Chen, Y.-G. Yoon, E. E. Jung, H. Babcock, J. S. Kang, S. Asano, H.-J. Suk, N. Pak, P. W. Tillberg, *Nat. Methods* **2017**, *14*, 593.